Analysis of Ocean Diurnal Variations from the Korean Geostationary Ocean Color Imager Measurements Using the DINEOF Method

Xiaoming Liu[1,2] and Menghua Wang[1,*]

[1]NOAA/NESDIS, Center for Satellite Applications and Research (STAR)
E/RA3, 5830 University Research Ct., College Park, MD 20740, USA

[2]CIRA, Colorado State University, Fort Collins, CO, USA

*Corresponding author: Menghua.Wang@noaa.gov

Estuarine, Coastal and Shelf Science

Revised on 6/14/2016

Running head: Diurnal variations from geostationary ocean color data

ABSTRACT

High-frequency images of the water diffuse attenuation coefficient at the wavelength of 490 nm (K_d(490)) derived from the Korean Geostationary Ocean Color Imager (GOCI) provide a unique opportunity to study diurnal variation of water turbidity in coastal regions of the Bohai Sea, Yellow Sea, and East China Sea. However, there are many missing pixels in the original GOCI-derived K_d(490) images due to clouds and various other reasons. Data Interpolating Empirical Orthogonal Function (DINEOF) is a method to reconstruct missing data in geophysical datasets based on the Empirical Orthogonal Function (EOF). It utilizes both temporal and spatial coherencies of data to infer a solution at the missing locations. In this study, the DINEOF is applied to GOCI-derived K_d(490) data in the Yangtze River mouth and the Yellow River mouth regions, and the DINEOF reconstructed K_d(490) data are used to fill in the missing pixels. In fact, DINEOF has been used to fill in gaps in ocean color chlorophyll-a and turbidity data from the Sea-viewing Wide Field-of-View Sensor (SeaWiFS), Moderate Resolution Imaging Spectroradiometer (MODIS), and Spinning Enhanced Visible and InfraRed Imager (SEVIRI) in previous studies. Our GOCI validation results show that the bias between the reconstructed data and the original K_d(490) value is quite small (< ~5%). The standard deviation of the reconstructed/original ratio is ~0.25 and ~0.30 for the mouths in the Yangtze River and Yellow River, respectively. In addition, GOCI high temporal resolution measurements in $K_d(490)$ can capture sub-diurnal variation due to the tidal forcing. The spatial patterns and temporal functions of the first three EOF modes are also examined. The first EOF mode characterizes the general mean spatial distribution of the region, while the second and third EOF modes represent the variations due to the tidal forcing in the region.

Keywords: GOCI, ocean color, EOF, DINEOF, $K_d(490)$, tide

1. Introduction

The Korean Geostationary Ocean Color Imager (GOCI) (*Cho et al.*, 2010; *Choi et al.*, 2012) is the first geostationary ocean color satellite sensor which was launched on June 27, 2010. GOCI covers an area of about 2500 × 2500 km^2 around the Korean Peninsula in the western Pacific region, including the Bohai Sea (BS), Yellow Sea (YS), and East China Sea (ECS), with the spatial resolution of 500 m (*Choi, et al.*, 2012). GOCI scans the area eight times a day hourly from local times of about 9:00 to 16:00. GOCI has six visible bands centered at the wavelengths of 412, 443, 490, 555, 660, and 680 nm and two near-infrared (NIR) bands at wavelengths of 745 and 865 nm for atmospheric correction (*Gordon and Wang*, 1994; *Wang et al.*, 2012). GOCI can monitor the regional marine environment changes and provide a variety of ocean optical, biological, and biogeochemical property products. Indeed, GOCI data can be used for various applications such as short- and long-term ocean environment monitoring, disaster and ocean hazard monitoring and prevention, ocean ecosystem and water quality evaluation and analysis, as well as intelligence and national security applications (*Cho, et al.*, 2010; *Choi, et al.*, 2012; *Doxaran et al.*, 2014; *Ryu et al.*, 2011; *Wang et al.*, 2013a; *Wang et al.*, 2014).

With highly temporal (hourly) measurements, GOCI has the capability to capture ocean diurnal variations due to wind, tide, and other physical forcing. In fact, in the BS, YS, and ECS, tidal forcing has a significant effect on the physical, biological, and suspended sediment conditions, and consequently on ocean properties as well (*Shi et al.*, 2011). The water diffuse attenuation coefficient at the wavelength 490 nm, $K_d(490)$ (or at the domain associated with photosynthetically available radiation (PAR) K_d(PAR)), is one of important satellite-derived ocean color products (*Lee et al.*, 2005; *Morel et al.*, 2007; *Son and Wang*, 2015; *Wang et al.*, 2009a). Indeed, parameter $K_d(490)$ measures the water turbidity, and it is highly correlated to the suspended sediment concentration in the water column over turbid waters (*Son and Wang*, 2012). In fact, using in situ data measured from the Chesapeake Bay, *Son and Wang* (2012) developed a linear algorithm to derive the suspended sediment concentration from satellite-measured $K_d(490)$ in the region. Therefore, $K_d(490)$ can be also used as a surrogate for the suspended sediment concentration in turbid estuaries and coastal regions, as well as for measuring water turbidity. GOCI-measured high frequency $K_d(490)$ data (*Wang, et al.*, 2013a) can be used to study the tidal effect on the suspended sediment transport, especially diurnal variations in the region (*Wang, et al.*, 2014). It should be noted that ocean biological and biogeochemical products such as $K_d(490)$ and chlorophyll-a concentration are derived from satellite-measured normalized water-leaving radiance spectra $nL_w(\lambda)$ (*Gordon*, 2005; *Morel and Gentili*, 1996; *Wang*, 2006) after carrying out atmospheric correction (*Gordon and Wang*, 1994; *IOCCG*, 2010; *Wang, et al.*, 2012).

However, there are generally many missing pixels in GOCI-derived $K_d(490)$ images for various reasons, mainly from cloud cover. It is useful to fill in the missing pixels before being used for some applications. A complete $K_d(490)$ coverage describing details in spatial distributions in the region is needed in order to understand some subtle ocean diurnal variations. The Empirical Orthogonal Function (EOF) analysis is a method to determine a set of orthogonal functions that characterizes the co-variability of time series for a set of grid points. It is often used to study possible spatial modes (patterns) of variability and how they change with time. Traditional EOF analysis operates on matrices and requires a complete array of data without gap in the matrices. The Data Interpolating Empirical Orthogonal Functions (DINEOF) (*Alvera-Azcarate et al.*, 2005; *Beckers and Rixen*, 2003) is an EOF-based technique developed to reconstruct missing data in geophysical datasets. It exploits the spatio-temporal coherency of the data to infer a value at the missing location, and has been successfully applied in various applications (*Alvera-Azcarate, et al.*, 2005; *Alvera-Azcarate et al.*, 2015; *Ganzedo et al.*, 2011; *Li and He*, 2014; *Mauri et al.*, 2007; *Mauri et al.*, 2008; *Nechad et al.*, 2011; *Sirjacobs et al.*, 2011; *Volpe et al.*, 2012).

It should be noted that the GOCI-derived ocean color products might have higher uncertainties for extremely turbid waters in the region due to the limitation using the NIR atmospheric correction algorithm (*Shi and Wang*, 2014). In fact, *Shi and Wang* (2014) have shown that for extremely turbid waters such as in the Hangzhou Bay during the winter season the red $nL_w(\lambda)$ data are saturated, and the NIR band data may have some limitations when used to derive ocean color products. In particular, $K_d(490)$ data may have larger uncertainties because of the saturation in red $nL_w(\lambda)$ data that are used to drive $K_d(490)$ product. For these cases, the shortwave infrared (SWIR)-based atmospheric correction (*Wang*, 2007; *Wang and Shi*, 2007) is required for ocean color data processing. However, in the summer season, waters in the GOCI-covered region are usually the least turbid (*Shi and Wang*, 2014) and the GOCI-derived ocean color products are generally reasonable (*Wang, et al.*, 2013a; *Wang, et al.*, 2014).

In this study, the DINEOF method is applied to high temporal frequency GOCI-measured $K_d(490)$ images in two coastal regions: the mouths of the Yangtze River and the Yellow River. The Yellow River and the Yangtze River deliver large amounts of sediments from the land to the ocean, and the annual sediment discharges for the two rivers are about 1.08×10^9 and 4.78×10^8 tons, respectively (*Saito et al.*, 2001). River sediment plumes form near the river mouth areas, and measurements of the sediment concentrations and their transport from the satellite are of special interest of research. The spatial coverage of the two areas of interests is shown in Fig. 1a, with enlarged GOCI-derived $K_d(490)$ images from the month of August (from 2011–2014) in the mouths of the Yellow River (Fig. 1b) and Yangtze River (Fig. 1c). The mouths of the Yangtze River and Yellow River are known as highly turbid coastal regions due to large amounts of suspended sediment from the rivers (*Shi and Wang*, 2012; 2014; *Zhang et al.*, 2010), and the tidal current has a strong effect on the suspended sediment transportation (*Shi, et al.*, 2011). The DINEOF reconstructed non-gap GOCI-measured $K_d(490)$ images and their validation results are presented. The EOF modes that characterize the tidal effects on the suspended sediment transportation in the region will also be discussed. It is noted that one of the main purposes for this study is the effective gap filling from satellite-measured $K_d(490)$ imagery for various applications.

2. Data and Methods

GOCI Level-1B data from March 2011 to November 2014 were obtained from the Korea Institute of Ocean Science and Technology (KIOST), and they were processed into ocean color products using the National Oceanic and Atmospheric Administration (NOAA) Multi-Sensor Level-1 to Level-2 (MSL12) ocean color data processing system. MSL12 was developed for the purpose of using a consistent and common data processing system to produce ocean color products from multiple satellite ocean color sensors, i.e., common algorithms in the data processing for all satellite ocean color sensors (*Wang and Franz*, 2000; *Wang et al.*, 2002). Specifically, NOAA-MSL12 is based on the SeaWiFS Data Analysis System (SeaDAS) version 4.6 with some important modifications and improvements. The improved MSL12 has been used to extensively process ocean color data from the Moderate Resolution Imaging Spectroradiometer (MODIS) on the satellite Aqua (*Wang et al.*, 2009b), the Visible Infrared Imaging Radiometer Suite (VIIRS) on the Suomi National Polar-orbiting Partnership (SNPP) (*Wang et al.*, 2013b), and GOCI (*Wang, et al.*, 2013a; *Wang, et al.*, 2012; *Wang, et al.*, 2014). Particularly, the SWIR-based atmospheric correction algorithm has been implemented in MSL12 and used for MODIS and VIIRS ocean color data processing in highly turbid coastal and inland waters, particularly over the GOCI-covered highly turbid China east coastal region (*Shi and Wang*, 2012; *Wang et al.*, 2007). In addition, MSL12 is an official NOAA VIIRS ocean color data processing system and has been used for routinely producing VIIRS global ocean color products (including global daily, 8-day, monthly, and climatology images) since VIIRS launch in October 2011 (*Wang, et al.*, 2013b) (http://www.star.nesdis.noaa.gov/sod/mecb/color/).

For the GOCI ocean color data processing, various parameters and lookup tables (LUTs), e.g., Rayleigh radiance LUTs, atmospheric diffuse transmittance LUTs, spectral solar irradiance data and ozone absorption coefficients, etc., have been generated and modified specifically to correspond to the GOCI eight spectral bands (*Wang, et al.*, 2013a; *Wang, et al.*, 2012). It is noted that these LUTs and various parameters were generated in the same way as those for MODIS-Aqua and VIIRS using the GOCI spectral response function data. In addition, to accommodate the requirement of the atmospheric correction for GOCI ocean color data processing, a regional NIR-$nL_w(\lambda)$ model has been used for atmospheric correction for ocean color data processing in the western Pacific region (*Wang, et al.*, 2012). Based on the regional empirical relationship between the NIR-$nL_w(\lambda)$ and $K_d(490)$, which is derived from long-term MODIS-Aqua measurements (2002–2009) using the SWIR-based ocean color data processing, an iterative scheme with the NIR-based atmospheric correction algorithm has been developed and has shown good results (*Wang, et al.*, 2013a). The details of the GOCI atmospheric correction and $K_d(490)$ algorithms, as well as some validation results, can be found in *Wang et al.* (2012) and *Wang et al.* (2013a).

GOCI-derived $K_d(490)$, like most satellite derived geophysical data, are three dimensional in nature: two-dimensional in space and one-dimensional in time. In this study, 61 consecutive days (August 1–September 30, 2013) of GOCI-measured $K_d(490)$ data were selected for the two areas of interest. In summer, daytime solar-zenith angles are smaller than those in winter, so that the hourly GOCI images in the early morning and late afternoon can be used. With eight consecutive images per day, there are 488 images for each of the two regions in 61 days, and it covers about 120 semidiurnal tide cycles and 4 spring-neap tide cycles, which are sufficient for studying the variations of $K_d(490)$ in the region due to tidal forcing. The spatial dimension of each image array is 400×350 pixels for the Yangtze River and 180×150 pixels for the Yellow River region (Fig. 1). For the DINEOF analysis, the three-dimensional array is reorganized as a two-dimensional array of space verses time (only ocean pixels are kept in the spatial dimension). As a result, the size of the two-dimension array is 95085×488 and 18325×488 for the Yangtze

River and Yellow River region, respectively. There are a total of 49.8% missing pixels for the Yangtze River region, and 45.3% missing pixels for the Yellow River region. However, the traditional EOF analysis can only be applied on a complete two-dimensional array without gap. For any ocean grid, there is a time series of 488 pixels. If any one or more pixels are missing in the time series of an ocean grid, we call it an incomplete grid. There are 82.0% and 95.6% of incomplete ocean grids for the Yangtze River region and the Yellow River region, respectively.

The DINEOF method (*Alvera-Azcarate, et al.*, 2005; *Beckers and Rixen*, 2003) is an EOF-based technique, which identifies and utilizes dominant spatial and temporal patterns in geophysical datasets to reconstruct missing data. The DINEOF procedure is summarized as follows. The initial data are obtained by subtracting the mean value from the entire data set and setting the missing data to zero. The EOF is then performed, and the missing data are replaced with the initial guess by reconstruction using the spatial and temporal functions of only the first EOF mode. The first EOF is recalculated iteratively using the previous best guess as the initial value of the missing data for the subsequent iteration until convergence. This procedure is then repeated with n ($n = 1, 2, 3,\ldots$) EOF modes. At each step, a cross-validation method is used to calculate the final optimum number of EOF modes to retain, so that the cross-validation error is minimized. It is noted that not all EOF modes are used in the final reconstruction, and the noise and the small-scale transient features in the high order EOF mode are removed from the reconstructed data. More details about the DINEOF technique can be found in *Beckers and Rixen* (2003) and *Alvera-Azcarate et al.* (2005).

3. Satellite Observations

3.1. DINEOF Reconstruction

The DINEOF method has been run independently on each of the two study regions. In the analysis, a cross-validation method is used to estimate the error between the reconstructed data and original true value in the GOCI $K_d(490)$ image, so that an optimal number of EOF modes are retained for data reconstruction. Table 1 summaries the number of EOF modes retained and the total variance explained, as well as the dimension of the two study regions.

Twelve (12) and fifteen (15) EOF modes are retained to reconstruct GOCI-derived $K_d(490)$ data for the Yangtze River and Yellow River region, respectively, and the missing/cloud pixels in the original GOCI $K_d(490)$ images are filled with reconstructed data. We use the following terminology for the three types of images: original image, reconstructed image, and filled image. Original image is the image derived directly from GOCI measurements, which contain missing data. Reconstructed image is calculated from the retained EOF modes using the DINEOF method (*Beckers and Rixen*, 2003). In the reconstructed image, all $K_d(490)$ data are reconstructed on every ocean pixel (including non-missing pixels). Reconstructed image has no-gap spatially, however, there are some small differences between reconstructed and original data even for non-missing pixels due to truncated EOF modes. The filled image is a combination of the original image and the reconstructed image, i.e., missing pixels are filled with reconstructed data and original data are kept for non-missing pixels.

As examples to demonstrate the capability of the DINEOF approach, Fig. 2 shows comparisons of original images and filled images for the two study areas. In the original image of the Yangtze River region (Fig. 2a), cloud covers most parts of the Yangtze River estuary and Hangzhou Bay on August 10, 2013 at 09:16 local time (white in Fig. 2a), and these missing data are filled with the DINEOF reconstructed values (Fig. 2b). With the spatio-temporal coherency of the data, the DINEOF reconstruction using the first 12 modes works very well to fill the missing pixels. The gap-free image in Fig. 2b provides a complete picture of $K_d(490)$ in the region. The missing maximum $K_d(490)$ values are recovered, and the transition between the reconstructed and original pixels are quite smooth. Similarly, for the Yellow River region, the original $K_d(490)$ image on August 23, 2013 at 12:16 local time does not provide detailed features near the Yellow River mouth, and there are lots of data missing in the open ocean (northeast of the Yellow River mouth) (Fig. 2c). In the filled image (Fig. 2d), the detailed structure of the

Yellow River sediment plume is recovered, providing a complete spatial $K_d(490)$ distribution in the region.

3.2. Validation of Reconstructed Data

To validate accuracy of the DINEOF data reconstruction method, a set of valid pixels are intentionally treated as "missing pixels," so that DINEOF-reconstructed data can be compared with the original true data (directly from GOCI measurements). This is in addition to the DINEOF internal cross-validation method, which is used to determine the optimal number of EOF modes to retain for the data reconstruction. Before the DINEOF process, about 1%, 5%, and 10% of valid (non-missing) pixels are on purposely removed from the original GOCI-derived $K_d(490)$ images for both study regions. The locations of these validation pixels are selected randomly using the random number generator in MatLab. After the DINEOF process, these data are reconstructed and compared with data from the original $K_d(490)$ images. Figure 3 shows the density scatter plots of the reconstructed data versus the original data of the validation pixels for three validation cases of each study region. Note that the maximum data number for each case in Fig. 3 is indicated in each plot, e.g., 2.5×10^4 for Fig. 3a, and the density plot uses the ratio to the maximum data number for each case. For the Yangtze River region, there are total of 38000, 190000, and 380000 validation pixels for the 1%, 5%, and 10% validation cases, respectively. The mean and standard deviation (STD) values of the "reconstructed to original ratio" are 1.024 and 0.255 for the case of 1% validation pixels (Fig. 3a), 1.024 and 0.262 for the case of 5% validation pixels (Fig. 3b), and 1.025 and 0.285 for the case of 10% validation pixels (Fig. 3c), respectively. Results show that the performance of the DINEOF reconstruction in the Yangtze River region is quite stable with different percentages of missing pixels, i.e., ratio of ~1.024 and STD of ~0.26. However, STD values increase with increase of missing data as expected. Similarly, for the Yellow River region, there are total of 7200, 36000, and 72000 validation pixels for the 1%, 5%, and 10% validation cases, respectively. The mean and STD values are 1.030 and 0.302 for the case of 1% validation pixels (Fig. 3d), 1.031 and 0.303 for the case of 5% validation pixels (Fig. 3e), and 1.041 and 0.527 for the case of 10% validation pixels (Fig. 3f), respectively. Again, the mean values (bias errors) are quite stable, and STD values increase with the increase of missing data, particularly for the 10% case. These comparisons show that the reconstructed data by the DINEOF method are quite accurate and reliable.

In the above validation cases with randomly selected missing pixels, there is no complete time series of pixels for validation. To validate a time series of the reconstructed data, a fixed location is selected on the boundary of the sediment plume, where the temporal variations are more significant, for each of the river mouth regions. The locations of the points are indicated in Fig. 2a for the Yangtze River region (marked "A") and Fig. 2b for the Yellow River region (marked "B"). Figure 4 shows the comparison of time series of the reconstructed data (solid lines) and the original data (circles) on a selected point for each region. The tidal water elevation data (dotted lines) at the locations A and B calculated using the Oregon State University Tidal Inversion Software (OTIS) (*Egbert et al.*, 1994; *Egbert and Erofeeva*, 2002) are also plotted in Fig. 4 for comparisons. For the Yangtze River dataset, both the original data and reconstructed data show the diurnal variations. On August 6, 2013, as the tidal elevation increases from about 09:16 local time at the location A, $K_d(490)$ decreases. The minimum $K_d(490)$ value occurs at about 12:16 local time as the tide reaches its maximum, and due to the tidal effect, the timing of the $K_d(490)$ minimum delays on each of the following days. This is because the region is dominated by the M_2 tide (*Shi, et al.*, 2011), which has a period of 12 hours and 25.2 minutes. Similarly, the minimum occurs at 13:16 local time on August 19, 2013 for the Yellow River region, and it gradually delays on each of the following days. On August 23, 2013, the minimum $K_d(490)$ occurs around 16:16 local time, which is also in phase with the period of the M_2 tide. The correlation coefficients (R) between the reconstructed and original $K_d(490)$ data are 0.848 and 0.965 for the location A (in the Yangtze River) and the location B (in the Yellow River), respectively. It is also noted that the DINEOF method removes some noises in the original data. For example, in the time series on August 10, 2013 of the Yangtze River region (Fig. 4e), the original data at 15:16 local time are obviously abnormal (probably due to the cloud contamination, e.g., stray light effect (*Jiang and Wang*, 2013)), and the DINEOF-reconstructed data remove the noise through the truncation of EOF modes. The high orders of the EOF modes are mostly contributed from the original data noise component.

3.3. Analysis of the Tidal Effect on the Suspended Sediment Transportation

GOCI-derived $K_d(490)$ data are closely related to suspended sediment concentration in the water column (*Son and Wang*, 2012), and the spatial and temporal variations in $K_d(490)$ can be used to study the suspended sediment transportation. Indeed, the suspended sediment transportation of the study areas is under strong influence of tidal forcing (*Shi, et al.*, 2011). GOCI measurements provide day-time high-frequency hourly $K_d(490)$ images, which can be used to study intra-tidal variations of suspended sediment concentration in the region.

Figure 5 shows eight filled $K_d(490)$ images of the Yangtze River mouth region on August 6, 2013. In general, $K_d(490)$ data are high near the coast in the Yangtze River estuary and Hangzhou Bay (> 2.0 m^{-1}), and low in the open ocean (< 2.0 m^{-1}). The spatial pattern of high $K_d(490)$ is very similar to the pattern of the Yangtze River plume (*Li and Rong*, 2012; *Shi and Wang*, 2010), which indicates that the high $K_d(490)$ is due to suspended sediment from the river discharge. The tidal current also transports the suspended sediments. On August 6, 2013, the suspended sediments moved towards the coast from 09:16 to 12:16 local time (the flood tide), and then away from the coast from 13:16 to 16:16 local time (the ebb tide). To show clearly the movement of suspended sediments, a fixed location is marked as a black crosshair in Fig. 5, so that the sediment movements relative to the fixed location can be investigated.

Figures 6 and 7 show the spatial patterns of the first three EOF modes for the Yangtze River mouth region and the corresponding temporal functions for the first three modes, respectively. Since a mean value of 2.070 m^{-1} was subtracted from the $K_d(490)$ data prior to the EOF process, the EOF modes shown are really anomalies. It is noted that the mean $K_d(490)$ value was computed from the all available GOCI-derived $K_d(490)$ pixels in the analysis (i.e., a mean value from all 488 images from both spatial and temporal data). In addition, each EOF mode is normalized by a so-called singular value, which measures the contribution of variance of each mode to the total variance (*Beckers and Rixen*, 2003). Therefore, results in Figs. 6 and 7 only depict the variation trend of each EOF mode in space and time, respectively. The first EOF mode accounts for 89.23% of the total variance, and it basically characterizes the general spatial distribution pattern in the region (Fig. 6a). The spatial distribution of the first EOF mode in $K_d(490)$ shows higher values in the coastal area than those in open oceans (as expected), and there is a sharp boundary which marks the limit of the river sediment plume near 122°E. Beyond the sediment plume, the $K_d(490)$ value decreases significantly. The variations of the second and third EOF modes are mainly confined along the boundary of the river plume (Figs. 6b and 6c), and they account for about 3.36% and 1.53% of the total variance, respectively. The temporal functions of the first three EOF modes (Fig. 7) all show the spring-neap tidal variations. The time series of tidal water elevation data at the location A calculated from OTIS are plotted as the background in Fig. 7. High values are found near the spring tides (August 7, 21, September 5, and 19), and minimums occur near the neap tides (August 17 and 31, September 15 and 29). In fact, the spring-neap tide cycle has about a 1–3 days lag behind moon phases (*El-Sabh et al.*, 1987). It has been reported that the spring-neap tide variation in the MODIS $K_d(490)$ data has a 2–3 days lag behind the moon phases in the western Pacific region, and it was attributed to two reasons (*Shi, et al.*, 2011). First, the effects of the seawater inertia and the friction against the seabed can cause the lag of the spring-neap tides by 1–3 days; and second, the sediment resuspension process in the water column due to grain size and settling velocity can also make a difference on the timing of water properties (e.g., $K_d(490)$) observed from the satellite.

In addition to the spring-neap cycle, the temporal EOF functions also show semi-diurnal variations, especially during the periods of August 4–14 and September 16–25 in Fig. 7. To demonstrate the semi-diurnal cycle more clearly, five days (August 6–10) of temporal functions of the first three EOF modes are shown in Fig. 8. The temporal function of the second EOF mode shows regular semi-diurnal variation (Fig. 8b). On the first day (August 6, 2013), the second EOF mode function starts to decrease from 09:16 local time. The function reaches the minimum at 12:16 local time, and then starts to increase (Fig. 8b). From August 6 to 10, the occurrence of the minimum gradually delays for about one hour on each day. On August 10, the minimum occurs at 16:16 local time (Fig. 8b). The gradual delay of the minimum on each day shows that the period of the variation in the temporal function of the second EOF mode is the same as that of the M_2 tide. The spatial pattern of the third EOF mode is similar to the second EOF mode (Fig. 6c). The temporal function of the third EOF mode also shows a semi-diurnal variation, but in a different phase (Fig. 8c). The combination of the first three EOF modes characterizes the tidal effect on the sediment transport in this region. In fact, the first three EOF modes can explain about 94.12% of the total $K_d(490)$ variations in the region.

It is noted that the temporal function depicts the variation of an EOF mode of the region as a whole. However, the observed and simulated co-tide and co-range charts of the semi-diurnal and diurnal components (M_2, S_2, K_1, and O_1) show that the tidal phase and tidal range are different from location to location in the BS and ECS (*Guo and Yanagi*, 1998). Therefore, the diurnal phase lag between the EOF temporal function and the location-based tidal elevation is also different from location to location in the region.

It is interesting to note that, in the second and third EOF modes, the variation in the coastal region north of Chongming Island (see Fig. 1c for the location) is out of phase with other regions on the boundary of the river plume. In Fig. 5, it can be seen that there is a big bulge of river sediment plume to the south of Chongming Island. But for the Yangtze River pathway north of the island, the river sediment is only transported halfway, and there is no sediment plume formed. In fact, the river sediment plume on the south is extended to the north around the island, and reaches even to its north shore. It seems that there is a patch of clear ocean water just north of Chongming Island, and on both its upstream and downstream sides are turbid river waters with high sediment concentration. The second and third EOF modes (Figs. 6b and 6c) characterize the interactions of the clear ocean water with turbid river waters on both sides. It can be seen in the spatial pattern of the second EOF mode, to the north of Chongming Island, there is a positive patch with a negative patch on both sides (Fig. 6b). When the temporal function of the second EOF mode increases, the $K_d(490)$ in the second EOF component increases in the positive patch, but decreases in the negative patches. When the temporal function of the second EOF mode decreases, the $K_d(490)$ in the second EOF component decreases in the positive patch, but increases in the negative patches. The feature of the third EOF mode is similar, but on an opposite phase (Fig. 6c). The combination of the second and the third EOF modes depicts an oscillation of the $K_d(490)$ near north of Chongming Island, and it would be interesting to use an ocean model to simulate the interaction of fresh and ocean water under the tidal forcing as a topic for the future study.

Similar to the Yangtze River case, there is a clear boundary of the river sediment plume near the Yellow River mouth. Within the sediment plume, $K_d(490)$ is larger than 2.0 m^{-1}, and $K_d(490)$ significantly decreases outside of the plume (< ~1.0 m^{-1}). Figures 9 and 10 show the spatial patterns of the first three EOF modes and the corresponding temporal functions in the Yellow River mouth, respectively. As for the Yangtze River mouth EOF analysis, the EOF modes are normalized by a set of singular values, and are $K_d(490)$ anomalies. The first EOF mode accounts for 82.68% of the total $K_d(490)$ variance, and it characterizes the general spatial distribution in $K_d(490)$ near the Yellow River mouth (Fig. 9a). The second and third EOF modes account for 6.18% and 2.60% of the total variance, respectively, and they characterize the variations of $K_d(490)$ on the boundary of the Yellow River plume (Figs. 9b and 9c). While the Yangtze River mouth is dominated by a regular semi-diurnal tidal cycle, the Yellow River mouth is mixed semi-diurnal cycle. The tidal range in the Yellow River mouth is also much smaller than that in the Yangtze River mouth. The temporal function of the second EOF mode shows a peak around 13:16 local time on the first day (August 19, 2013), and the occurrence of the peak has about one-hour delay on each day due to the semidiurnal tide (Fig. 10b). The third EOF mode is similar to the second mode, but with a lag in phase (Fig. 10c). Since the DINEOF processes are performed separately on the Yellow River mouth and Yangtze River mouth, the order of the EOF modes are not necessarily consistent between the two regions. In both regions, the first EOF mode is the most dominate (~80–90%), and the second and third EOF modes are on the same order of significance (~1–7%) in the both regions. The relative importance of the second and third modes only depends on the percentage of variance explained, and it could be different for different regions. The combination of the second and the third modes characterizes the tidal effect on the sediment transport in this region. The first three modes explain 91.46% of total $K_d(490)$ variations in the region.

4. Discussions and Summary

High-frequency $K_d(490)$ images from GOCI provide a unique opportunity to study diurnal variation of the water turbidity in the Yangtze River mouth and Yellow River mouth regions. However, there are often missing pixels in the original GOCI-derived $K_d(490)$ images. In this study, the DINEOF method is used to fill the missing pixels in $K_d(490)$ images, and is applied to 61 days (488 images in August and September of 2013) of GOCI-derived $K_d(490)$ data in the Yangtze River mouth region and Yellow River mouth region. An optimal number of EOF modes are retained for the data reconstruction, and missing pixels are filled with the reconstructed data. It has been demonstrated that the DINEOF method has the capability to retrieve the detailed structure of river suspended sediment plume in the two regions, and the transitions between the "filled" and "original" pixels are also found to be very smooth.

To validate the data reconstruction, about 1%, 5%, and 10% of valid pixels in the original datasets are intentionally treated as "missing pixels" for each of the two regions, so that the reconstructed data can be compared with original "true values." The validation results show that the bias between the reconstructed data and the original value is generally small, and the average of the reconstructed/original ratio is ~1.024 and ~1.035 for the Yangtze River mouth and Yellow River mouth region, respectively. The STD values of the "reconstructed/original" ratio are ~0.260 and ~0.377 for the corresponding regions, increasing with the increase of "missing pixels." However, it should be noted that the original $K_d(490)$ images are noisy. The DINEOF only keeps a limited (optimal) number of EOF modes for data reconstruction. The truncated EOF modes (modes that are discarded and not used for reconstruction images) are mostly data noise or lower order transient physical processes, and thus are excluded during the DINEOF data processing. This could also increase the STD of the reconstructed/original ratio.

The spatial and temporal functions of the first three EOF modes are examined. For both of the two study regions, the first EOF mode characterizes the general mean distribution of the water turbidity. The $K_d(490)$ value is high near the coast in the river sediment plume, and decreases significantly outside of the plume. The second and third EOF modes characterize the variation due to the tidal forcing, where the most significant changes occurs near the boundary of the sediment plume. Spring-neap cycles are found in the temporal functions of the first three EOF modes. In the temporal function of the second and the third EOF modes, the daily peak value delays every day for about 50 minutes, which is in phase with the period of the M_2 tide. The first three EOF modes explain more than 90% of variations for both study regions.

Acknowledgements

The GOCI Level-1B data used in this study were provided by Korean Institute of Ocean Science and Technology (KIOST). We thank three anonymous reviewers for their useful comments. The views, opinions, and findings contained in this paper are those of the authors and should not be construed as an official NOAA or U.S. Government position, policy, or decision.

References

Alvera-Azcarate, A., Barth, A., Rixen, M., and Beckers, J. (2005), Reconstruction of incomplete oceanographic data sets using Empirical Orthogonal Functions. Application to the Adriatic Sea, *Ocean Modeling*, *9*, 325–346.

Alvera-Azcarate, A., Vanhellemont, Q., Ruddick, K. G., Barth, A., and Beckers, J.-M. (2015), Analysis of high frequency geostationary ocean colour data using DINEOF, *Estuarine, Coastal and Shelf Science*, *159*, 28–36.

Beckers, J., and Rixen, M. (2003), EOF calculations and data filling from incomplete oceanographic data sets, *J. Atmos. Ocean Technol.*, *20*, 1839–1856.

Cho, S., Ahn, Y. H., Ryu, J. H., Kang, G., and Youn, H. (2010), Development of Geostationary Ocean Color Imager (GOCI), *Korean J. Remote Sens.*, *26*, 157–165.

Choi, J. K., Park, Y. J., Ahn, J. H., Lim, H. S., Eom, J., and Ryu, J. H. (2012), GOCI, the world's first geostationary ocean color observation satellite, for the monitoring of temporal variability in coastal water turbidity, *J. Geophys. Res.*, *117*, C09004, doi: 10.1029/2012JC008046.

Doxaran, D., Lamquin, N., Park, Y. J., Mazeran, C., Ryu, J. H., Wang, M., and Poteau, A. (2014), Retrieval of the seawater reflectance for suspended solids monitoring in the East China Sea using MODIS, MERIS and GOCI satellite data, *Remote Sens. Environ.*, *146*, 36–48.

Egbert, G. D., Bennett, A. F., and Foreman, M. G. G. (1994), TOPEX/POSEIDON tides estimated using a global inverse model, *J. Geophys. Res.*, *99*, 24821–24852.

Egbert, G. D., and Erofeeva, S. Y. (2002), Efficient inverse modeling of barotropic ocean tides, *J. Amos. Oceanic Technol.*, *19*, 183–204.

El-Sabh, M. I., Murty, T. S., and Cote, R. (1987), Variations of the age of tides in the global oceans, *Marine Geodesy*, *11*, 153–171.

Ganzedo, U., Alvera-Azcarate, A., Esnaola, G., Ezcurra, A., and Saenz, J. (2011), Reconstruction of sea surface temperature by means of DINEOF. A case study during the fishing season in the Bay of Biscay, *Int. J. Remote Sens.*, *32*, 933–950.

Gordon, H. R. (2005), Normalized water-leaving radiance: revisiting the influence of surface roughness, *Appl. Opt.*, *44*, 241–248.

Gordon, H. R., and Wang, M. (1994), Retrieval of water-leaving radiance and aerosol optical thickness over the oceans with SeaWiFS: A preliminary algorithm, *Appl. Opt.*, *33*, 443–452.

Guo, X., and Yanagi, T. (1998), Three-dimensional structure of tidal current in the East China Sea and Yellow Sea, *J. Oceanography*, *54*, 651–668.

IOCCG (2010), Atmospheric Correction for Remotely-Sensed Ocean-Colour Products, Wang, M. (Ed.), *Reports of International Ocean-Color Coordinating Group,* No. 10, IOCCG, Dartmouth, Canada.

Jiang, L., and Wang, M. (2013), Identification of pixels with stray light and cloud shadow contaminations in the satellite ocean color data processing, *Appl. Opt.*, *52*, 6757–6770.

Lee, Z. P., Darecki, M., Carder, K., Davis, C., Stramski, D., and Rhea, W. (2005), Diffuse attenuation coefficient of downwelling irradiance: An evaluation of remote sensing methods, *J. Geophys. Res.*, *110*, C02017, doi:10.1029/2004JC002573.

Li, M., and Rong, Z. (2012), Effects of tides on freshwater and volume transports in the Changjiang River plume, *J. Geophys. Res. Oceans*, *117*, C06027, doi: 10.1029/2011JC007716.

Li, Y., and He, R. (2014), Spatial and temporal variability of SST and ocean color in the Gulf of Maine based on cloud-free SST and chlorophyll reconstructions in 2003–2012, *Remote Sens. Environ.*, *144*, 98–108.

Mauri, E., Poulain, P. M., and Juznic-Zontac, Z. (2007), MODIS chlorophyll variability in the northern Adriatic Sea and relationship with forcing parameters, *J. Geophys. Res.*, *112*, C03S11, http://dx.doi.org/10.1029/2006JC003545.

Mauri, E., Poulain, P. M., and Notarstefano, G. (2008), Spatial and temporal variability of the sea surface temperature in the Gulf of Trieste between January 2000 and December 2006, *J. Geophys. Res.*, *113*, C10012, doi: 10.1029/2007JC004537.

Morel, A., and Gentili, G. (1996), Diffuse reflectance of oceanic waters. III. Implication of bidirectionality for the remote-sensing problem, *Appl. Opt.*, *35*, 4850–4862.

Morel, A., Huot, Y., Gentili, B., Werdell, P. J., Hooker, S. B., and Franz, B. A. (2007), Examining the consistency of products derived from various ocean color sensors in open ocean (Case 1) waters in the perspective of a multi-sensor approach, *Remote Sens. Environ.*, *111*, 69–88.

Nechad, B., Alvera-Azcarate, A., Ruddick, K., and Greenwood, N. (2011), Reconstruction of MODIS total suspended matter time series maps by DINEOF and validation with autonomous platform data, *Ocean Dynamics*, *61*, 19205–11214.

Ryu, J. H., Choi, J. K., Eom, J., and Ahn, J. H. (2011), Temporal variation in Korean coastal waters using Geostationary Ocean Color Imager, *J. Coastal Research*, *64*, 1731–1735.

Saito, Y., Yang, Z., and Hori, K. (2001), The Huanghe (Yellow River) and Changjiang (Yangtze River) deltas: a review on their characteristics, evolution and sediment discharge during the Holocene, *Geomorphology*, *41*, 219–231.

Shi, W., and Wang, M. (2010), Satellite observations of the seasonal sediment plume in central East China Sea, *J. Mar. Syst.*, *82*, 280–285.

Shi, W., and Wang, M. (2012), Satellite views of the Bohai Sea, Yellow Sea, and East China Sea, *Prog. Oceanogr.*, *104*, 35–45.

Shi, W., and Wang, M. (2014), Ocean reflectance spectra at the red, near-infrared, and shortwave infrared from highly turbid waters: A study in the Bohai Sea, Yellow Sea, and East China Sea, *Limnol. Oceanogr.*, *59*, 427–444.

Shi, W., Wang, M., and Jiang, L. (2011), Spring-neap tidal effects on satellite ocean color observations in the Bohai Sea, Yellow Sea, and East China Sea, *J. Geophys. Res.*, *116*, C12032, http://dx.doi.org/10.1029/2010JC007234.

Sirjacobs, D., Alvera-Azcarate, A., Barth, A., Lacroix, G., Park, Y., Nechad, B., Ruddick, K., and Beckers, J. (2011), Cloud filling of ocean color and sea surface temperature remote sensing products over the Southern North Sea by the data interpolating empirical orthogonal functions methodology, *J. Sea Res.*, *65*, 114–130.

Son, S., and Wang, M. (2012), Water properties in Chesapeake Bay from MODIS-Aqua measurements, *Remote Sens. Environ.*, *123*, 163–174.

Son, S., and Wang, M. (2015), Diffuse attenuation coefficient of the photosynthetically available radiation Kd(PAR) for global open ocean and coastal waters, *Remote Sens. Environ.*, *159*, 250–258.

Volpe, G., Nardelli, B. B., Cipollini, P., Santoleri, R., and Robinson, I. S. (2012), Seasonal to interannual phytoplankton response to physical processes in the Mediterranean Sea from satellite observations, *Remote Sens. Environ.*, *117*, 223–235.

Wang, M. (2006), Effects of ocean surface reflectance variation with solar elevation on normalized water-leaving radiance, *Appl. Opt.*, *45*, 4122–4128.

Wang, M. (2007), Remote sensing of the ocean contributions from ultraviolet to near-infrared using the shortwave infrared bands: simulations, *Appl. Opt.*, *46*, 1535–1547.

Wang, M., Ahn, J. H., Jiang, L., Shi, W., Son, S., Park, Y. J., and Ryu, J. H. (2013a), Ocean color products from the Korean Geostationary Ocean Color Imager (GOCI), *Opt. Express*, *21*, 3835–3849.

Wang, M., and Franz, B. A. (2000), Comparing the ocean color measurements between MOS and SeaWiFS: A vicarious intercalibration approach for MOS, *IEEE Trans. Geosci. Remote Sens.*, *38*, 184–197.

Wang, M., Isaacman, A., Franz, B. A., and McClain, C. R. (2002), Ocean color optical property data derived from the Japanese Ocean Color and Temperature Scanner and the French Polarization and Directionality of the Earth's Reflectances: A comparison study, *Appl. Opt.*, *41*, 974–990.

Wang, M., Liu, X., Tan, L., Jiang, L., Son, S., Shi, W., Rausch, K., and Voss, K. (2013b), Impact of VIIRS SDR performance on ocean color products, *J. Geophys. Res. Atmos.*, *118*, 10347–10360, doi:10.1002/jgrd.50793.

Wang, M., and Shi, W. (2007), The NIR-SWIR combined atmospheric correction approach for MODIS ocean color data processing, *Opt. Express*, *15*, 15722–15733.

Wang, M., Shi, W., and Jiang, L. (2012), Atmospheric correction using near-infrared bands for satellite ocean color data processing in the turbid western Pacific region, *Opt. Express*, *20*, 741–753.

Wang, M., Son, S., Jiang, L., and Shi, W. (2014), Observations of ocean diurnal variations from the Korean Geostationary Ocean Color Imager (GOCI), *Proc. SPIE*, *9111*, 911102, http://dx.doi.org/911110.911117/911112.2053476.

Wang, M., Son, S., and L. W. Harding, J. (2009a), Retrieval of diffuse attenuation coefficient in the Chesapeake Bay and turbid ocean regions for satellite ocean color applications, *J. Geophys. Res.*, *114*, C10011, http://dx.doi.org/10.1029/2009JC005286.

Wang, M., Son, S., and Shi, W. (2009b), Evaluation of MODIS SWIR and NIR-SWIR atmospheric correction algorithm using SeaBASS data, *Remote Sens. Environ.*, *113*, 635–644.

Wang, M., Tang, J., and Shi, W. (2007), MODIS-derived ocean color products along the China east coastal region, *Geophy. Res. Lett.*, *34*, L06611, http://dx.doi.org/10.1029/2006GL028599.

Zhang, M., Tang, J., Dong, Q., Song, Q., and Ding, J. (2010), Retrieval of total suspended matter concentration in the Yellow and East China Seas from MODIS imagery, *Remote Sens. Environ.*, *114*, 392–403.

Figure Captions

Figure 1. Location and GOCI-derived climatology $K_d(490)$ images (from the month of August 2011–2014) for the study regions: (a) area map of marginal seas on the China east coast, (b) $K_d(490)$ image in the Yellow River mouth, and (c) $K_d(490)$ image in the Yangtze River mouth.

Figure 2. Examples of original $K_d(490)$ images (a and c) and filled $K_d(490)$ images (b and d). Panels (a) and (b) are from the Yangtze River mouth region on August 10, 2013 at 09:00 local time, and panels (c) and (d) are from the Yellow River mouth region on August 23, 2013 at 12:00 local time.

Figure 3. Scatter and density plots of the reconstructed versus original $K_d(490)$ values for the Yangtze River mouth (panels a, b, and c), and the Yellow River mouth (panels d, e, and f). Panels a and d have 1% validation pixels, panels b and e have 5% validation pixels, and panels c and f have 10% validation pixels. The maximum numbers of pixels indicated for panels a, b, and c are 2.5×10^4, 1.2×10^5, and 2.0×10^5, respectively. The maximum numbers of pixels indicated for panels d, e, and f are 3.5×10^3, 1.6×10^4, and 3.0×10^4, respectively.

Figure 4. Time series (diurnal variation) of $K_d(490)$ for the original and reconstructed pixels, as well as the tide elevation (scale noted in right), for the locations A and B marked in Fig. 2a and 2c, respectively, for the Yangtze River mouth for August 6–10, 2013 (a–e) and the Yellow River mouth for August 19–23, 2013 (f–j).

Figure 5. Example of eight filled consecutive $K_d(490)$ images at 09:00 to 16:00 local time hourly (a–h) for the Yangtze River mouth region on August 6, 2013.

Figure 6. The spatial pattern functions of the first three EOF modes (a–c) in $K_d(490)$ for the Yangtze River mouth region.

Figure 7. The temporal functions (black lines) of August and September 2013 correspond to the first three EOF modes (a–c) as shown in Fig. 6. The background lines are tidal elevation data at the location A in Fig. 2a calculated from the OTIS.

Figure 8. Same as Fig. 7, but only shows the temporal functions of 5 days, August 6–10, 2013.

Figure 9. The spatial patterns of the first three EOF modes (a–c) in $K_d(490)$ for the Yellow River mouth region.

Figure 10. The temporal functions corresponding to the first three EOF modes (a–c) as shown in Fig. 9 for the Yellow River mouth region.

Table 1. The latitude/longitude limits, spatial coverage, number of pixels, incomplete grid, percentage of missing data, number of EOF modes retained, and variance explained by the retained EOF modes.

Region	Lat/Lon Limits	Spatial Size (pixels)	Number of Pixels	Incomplete Grid (%)	Missing Data (%)	EOF Modes Retained	Variance Explained (%)
Yangtze River Mouth	30°–31.7°N 121.5°–122.5°E	400×350	95085	82.0	49.8	12	98.66
Yellow River Mouth	37.4°–38.1°N 118.8°–119.5°E	180×150	18325	95.6	45.3	15	98.99

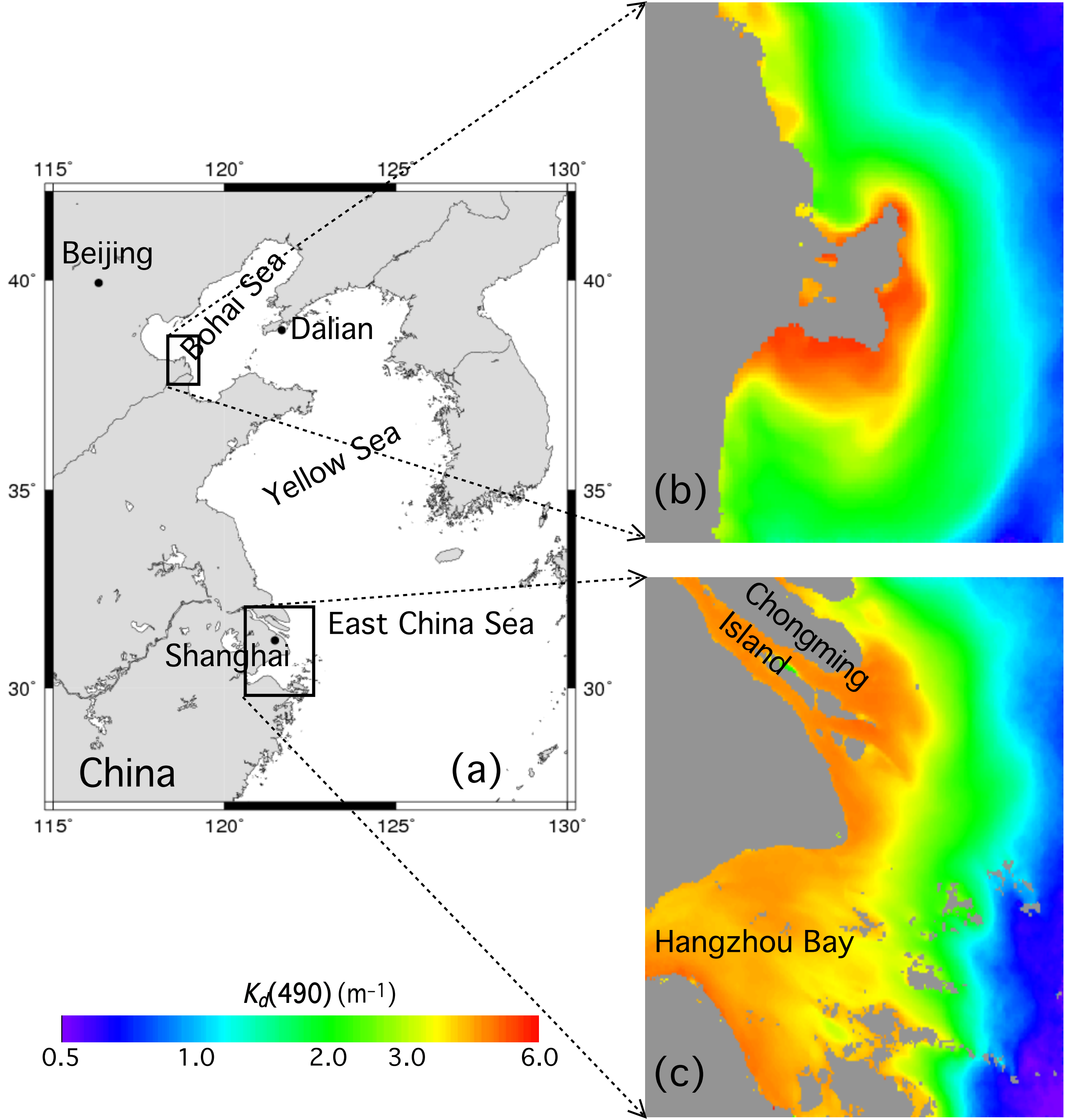

115°
120°
125°
130°
40°
35°
30°
Beijing
Bohai Sea
Dalian
Yellow Sea
East China Sea
Shanghai
China
(a)
(b)
(c)
Chongming
Island
Hangzhou Bay
$K_d(490)$ (m-1)
0.5
1.0
2.0
3.0
6.0

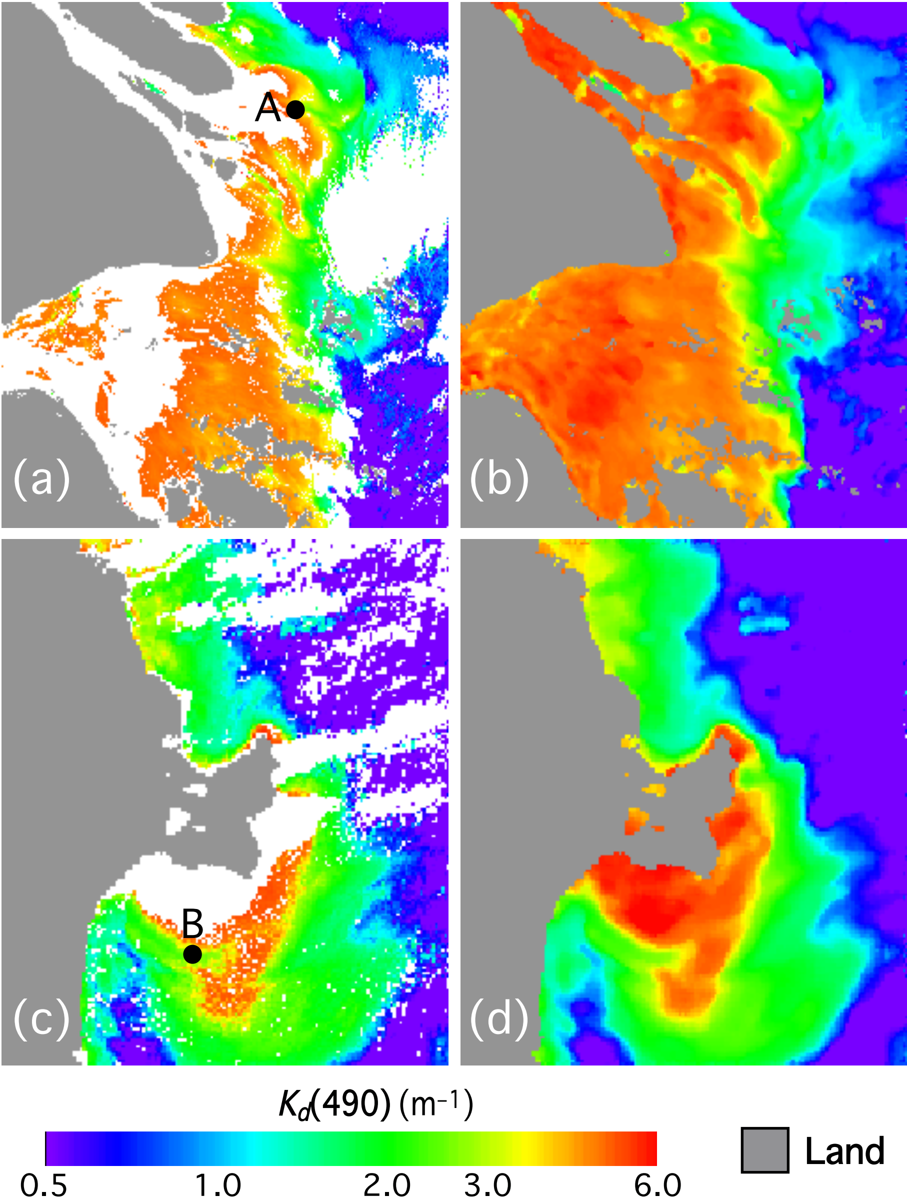
A
B
(a)
(b)
(c)
(d)
$K_d(490)$ (m^{-1})
0.5
1.0
2.0
3.0
6.0
Land

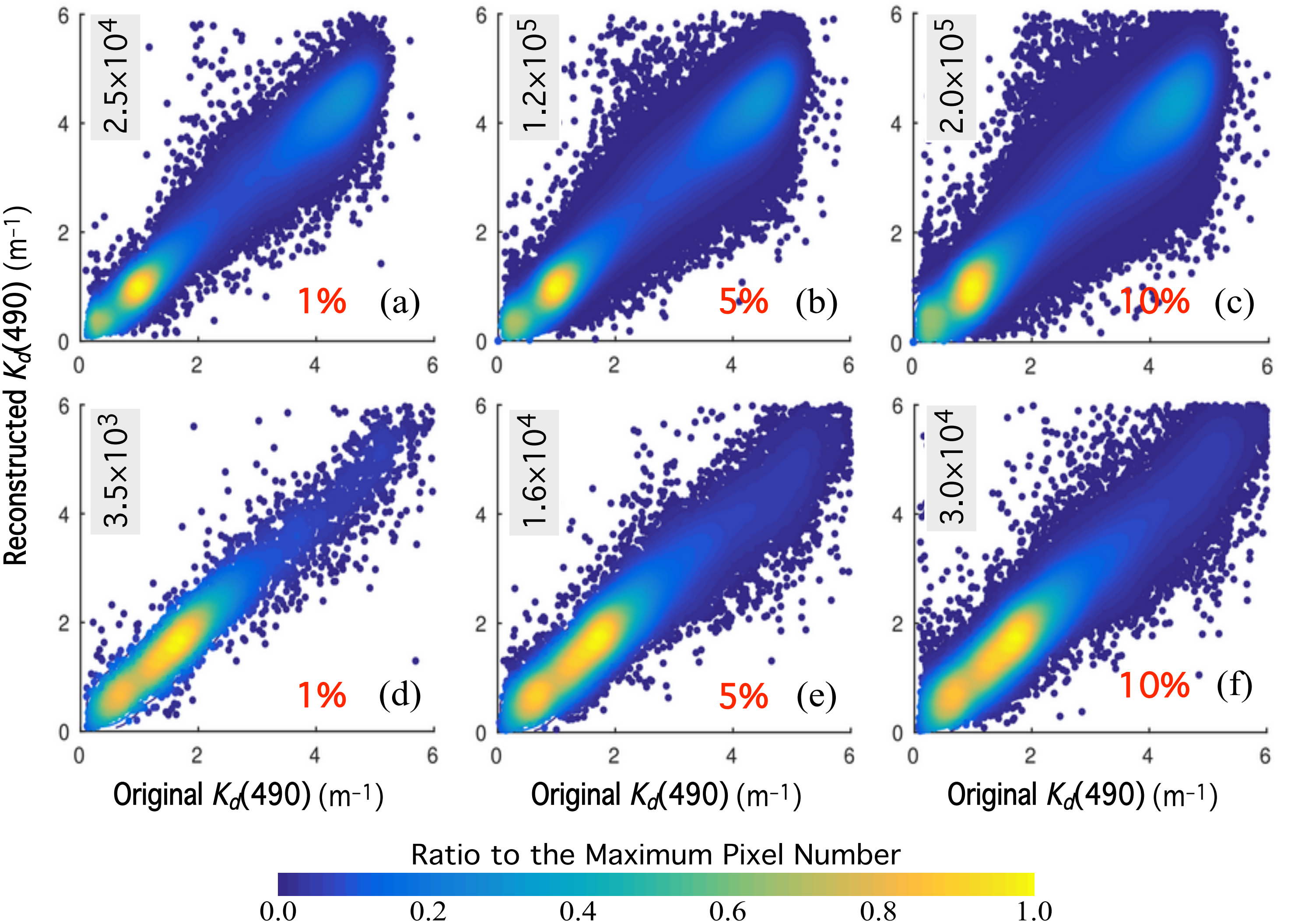

2.5×10^4
1%
(a)
1.2×10^5
5%
(b)
2.0×10^5
10%
(c)
3.5×10^3
1%
(d)
1.6×10^4
5%
(e)
3.0×10^4
10%
(f)
Reconstructed Kd(490) (m-1)
Original Kd(490) (m-1)
Original Kd(490) (m-1)
Original Kd(490) (m-1)
Ratio to the Maximum Pixel Number
0.0
0.2
0.4
0.6
0.8
1.0

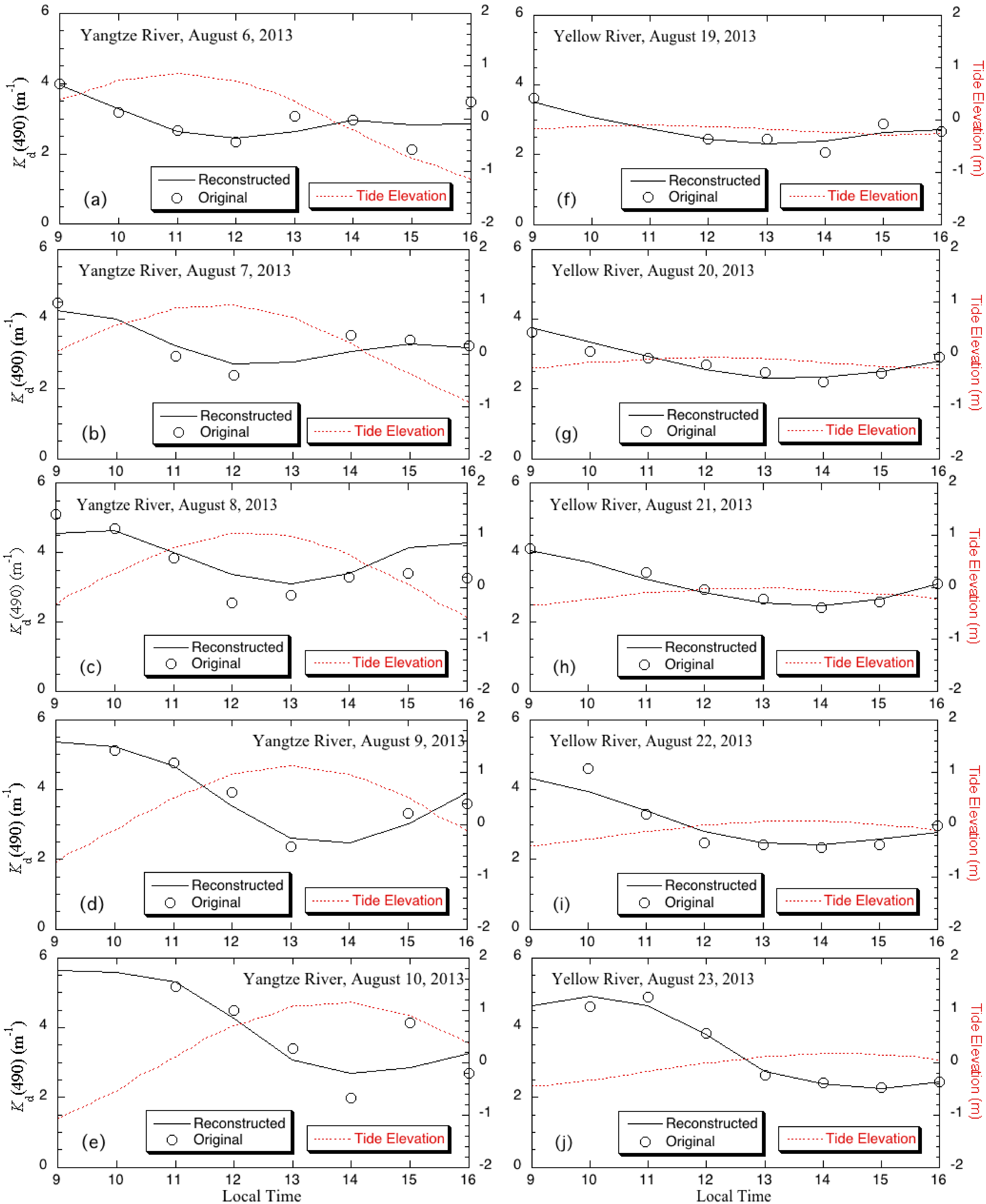

Yangtze River, August 6, 2013
Yangtze River, August 7, 2013
Yangtze River, August 8, 2013
Yangtze River, August 9, 2013
Yangtze River, August 10, 2013
Yellow River, August 19, 2013
Yellow River, August 20, 2013
Yellow River, August 21, 2013
Yellow River, August 22, 2013
Yellow River, August 23, 2013
(a)
(b)
(c)
(d)
(e)
(f)
(g)
(h)
(i)
(j)
Reconstructed
Original
Tide Elevation
$K_d(490)$ (m^{-1})
Tide Elevation (m)
Local Time

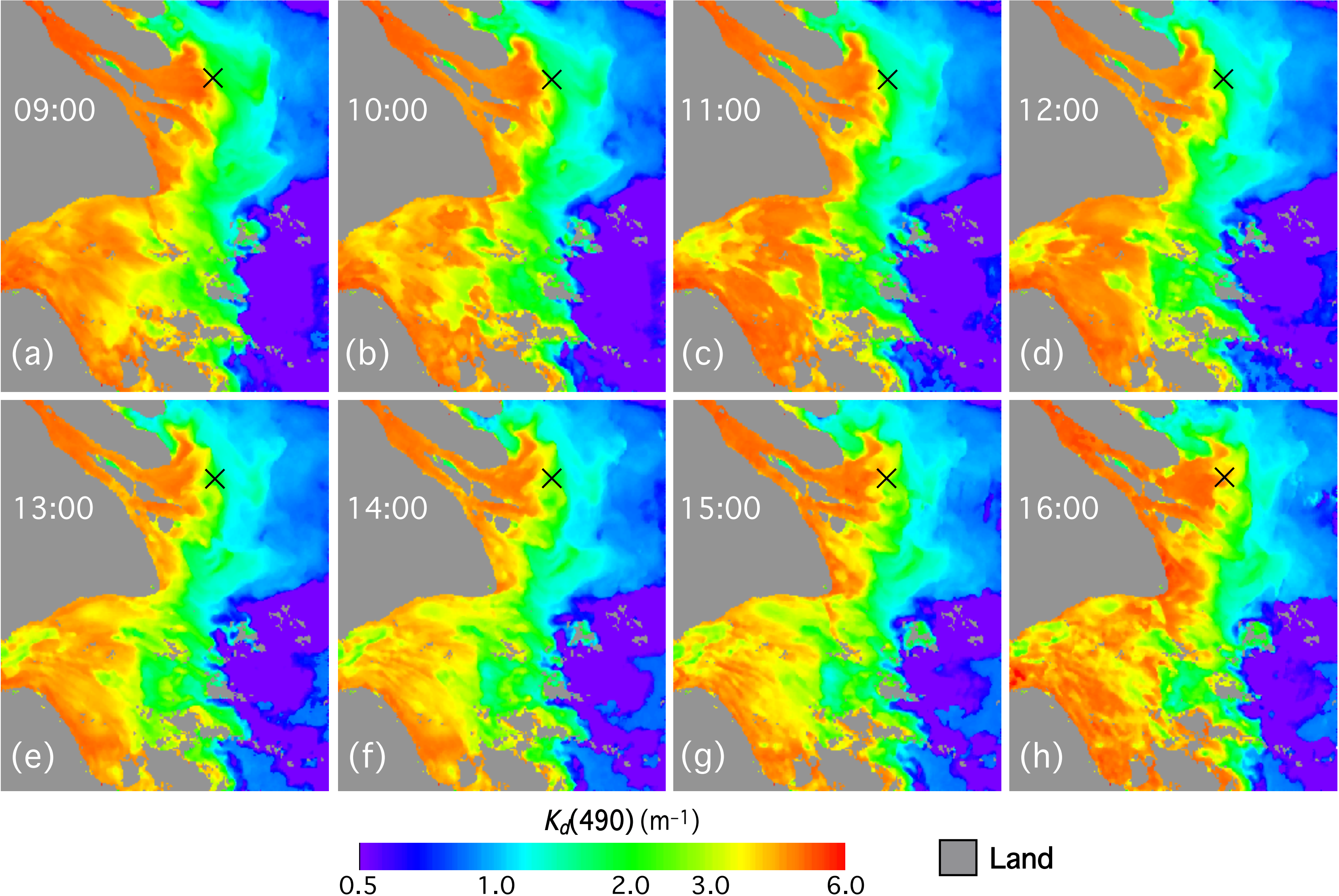

09:00
(a)
10:00
(b)
11:00
(c)
12:00
(d)
13:00
(e)
14:00
(f)
15:00
(g)
16:00
(h)
$K_d(490)$ (m^{-1})
0.5
1.0
2.0
3.0
6.0
Land

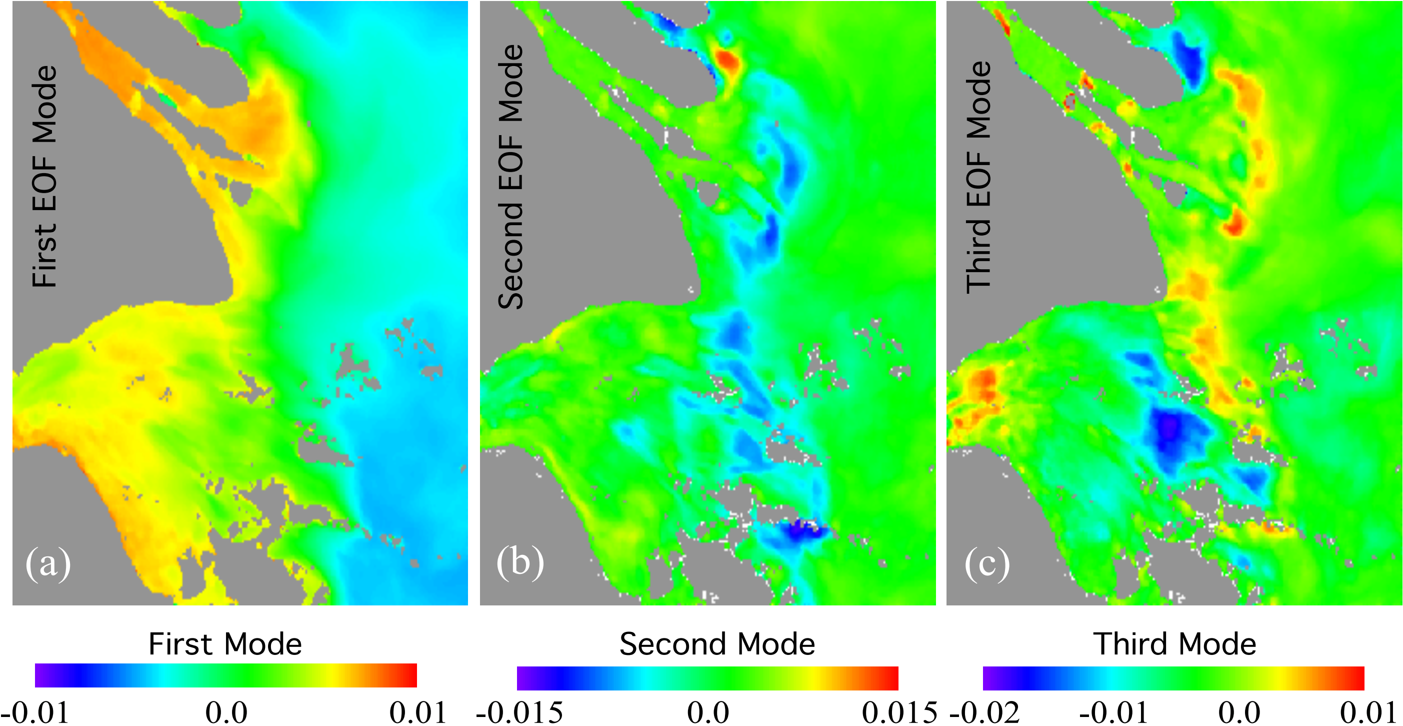
First EOF Mode
Second EOF Mode
Third EOF Mode
(a)
(b)
(c)
First Mode
-0.01
0.0
0.01
Second Mode
-0.015
0.0
0.015
Third Mode
-0.02
-0.01
0.0
0.01

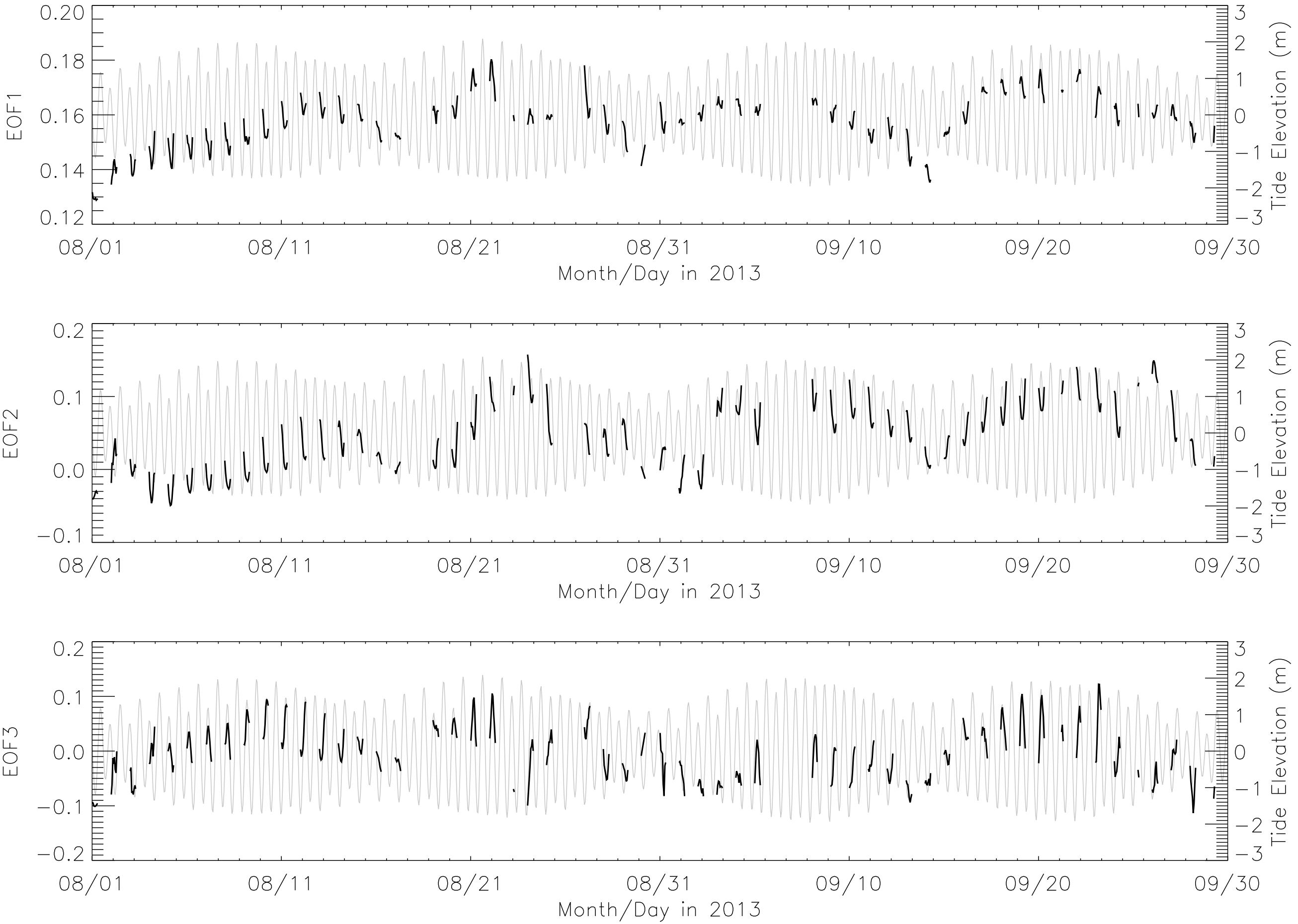
EOF1
0.20
0.18
0.16
0.14
0.12
Tide Elevation (m)
3
2
1
0
−1
−2
−3
08/01
08/11
08/21
08/31
09/10
09/20
09/30
Month/Day in 2013
EOF2
0.2
0.1
0.0
−0.1
Tide Elevation (m)
08/01
08/11
08/21
08/31
09/10
09/20
09/30
Month/Day in 2013
EOF3
0.2
0.1
0.0
−0.1
−0.2
Tide Elevation (m)
08/01
08/11
08/21
08/31
09/10
09/20
09/30
Month/Day in 2013

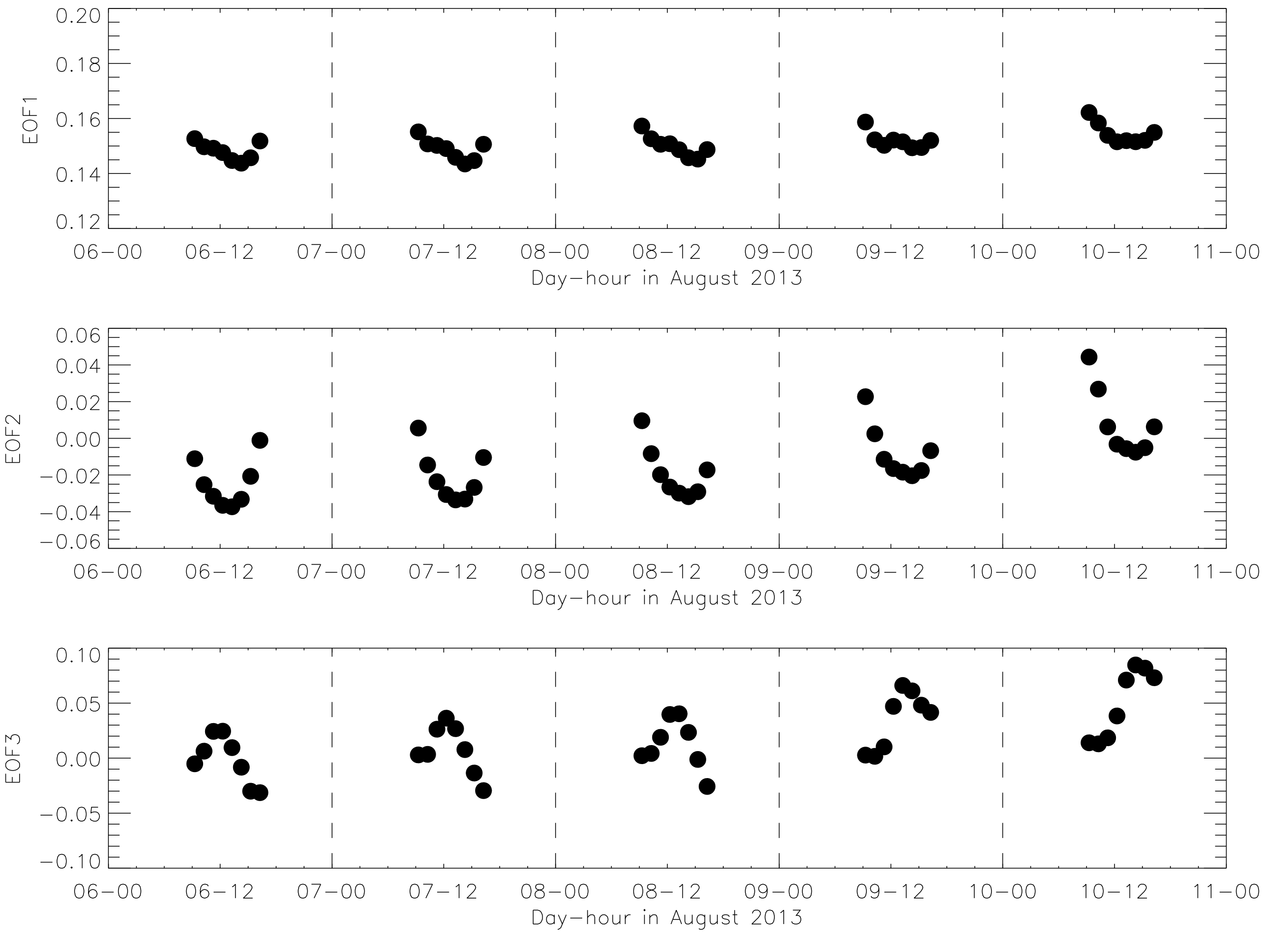
EOF1
0.20
0.18
0.16
0.14
0.12
EOF2
0.06
0.04
0.02
0.00
−0.02
−0.04
−0.06
EOF3
0.10
0.05
0.00
−0.05
−0.10
06−00
06−12
07−00
07−12
08−00
08−12
09−00
09−12
10−00
10−12
11−00
Day−hour in August 2013

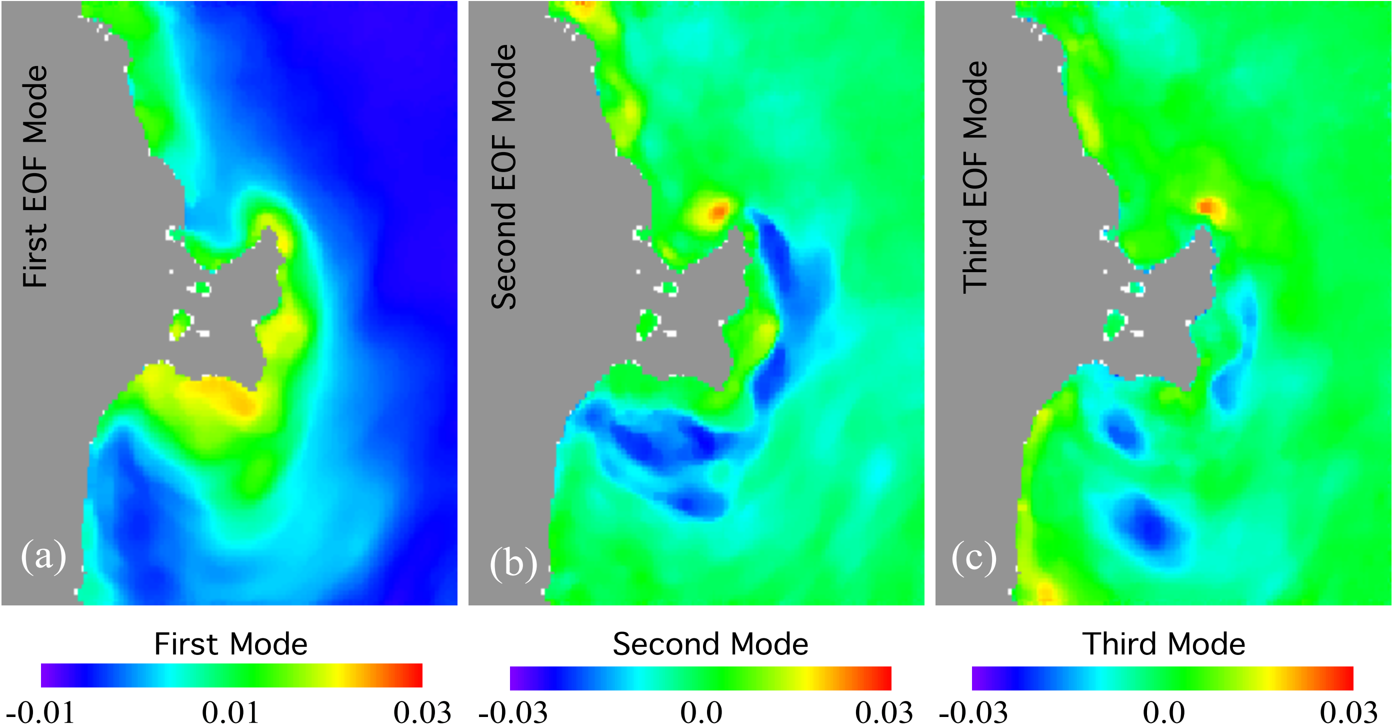
First EOF Mode
Second EOF Mode
Third EOF Mode
(a)
(b)
(c)
First Mode
-0.01
0.01
0.03
Second Mode
-0.03
0.0
0.03
Third Mode
-0.03
0.0
0.03

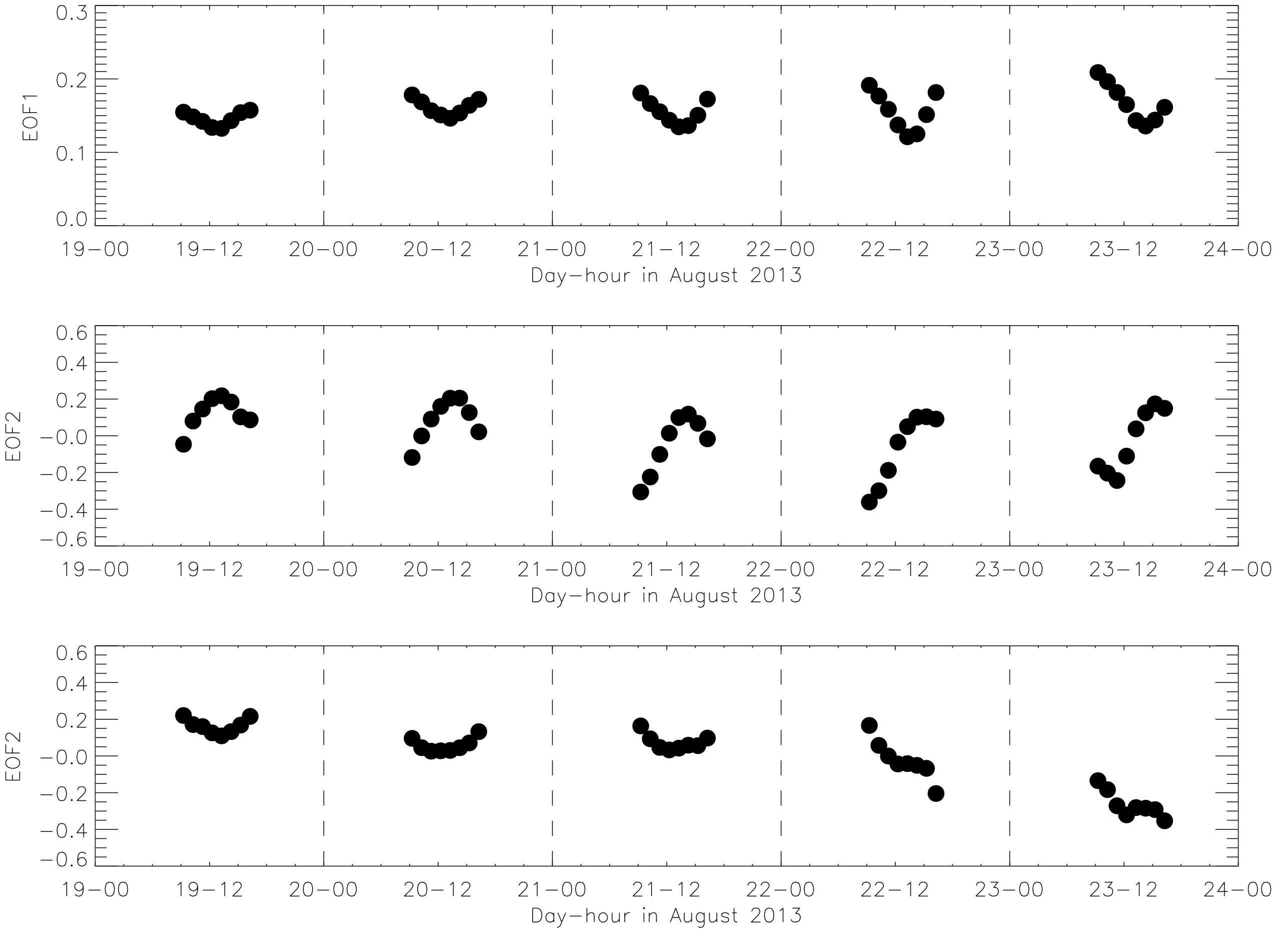

EOF1
0.3
0.2
0.1
0.0
19−00
19−12
20−00
20−12
21−00
21−12
22−00
22−12
23−00
23−12
24−00
Day−hour in August 2013
EOF2
0.6
0.4
0.2
−0.0
−0.2
−0.4
−0.6
19−00
19−12
20−00
20−12
21−00
21−12
22−00
22−12
23−00
23−12
24−00
Day−hour in August 2013
EOF2
0.6
0.4
0.2
−0.0
−0.2
−0.4
−0.6
19−00
19−12
20−00
20−12
21−00
21−12
22−00
22−12
23−00
23−12
24−00
Day−hour in August 2013